

A quasi-uniform acoustic leaky-wave antenna: Analysis, design and experimental validation

Downloaded from: https://research.chalmers.se, 2026-11-24 12:38 UTC

Citation for the original published paper (version of record):

Forssén, J., Martinez-Vicente, P., Algaba Brazalez, A. et al (2026). A quasi-uniform acoustic leaky-wave antenna: Analysis, design and experimental validation. Journal of the Acoustical Society of America, 160(4): 2988-3002. http://dx.doi.org/10.1121/10.0046796

N.B. When citing this work, cite the original published paper.

research.chalmers.se offers the possibility of retrieving research publications produced at Chalmers University of Technology. It covers all kind of research output: articles, dissertations, conference papers, reports etc. since 2004. research.chalmers.se is administrated and maintained by Chalmers Library

(article starts on next page)

The Journal of the Acoustical Society of America

OCTOBER 13 2026

A quasi-uniform acoustic leaky-wave antenna: Analysis, design and experimental validation

Jens Forssén ; Pablo-Antonio Martínez-Vicente; Astrid Algaba-Brazález; Matthew Polidano; José-Luis Gómez-Tornero

Check for updates

J. Acoust. Soc. Am. 160, 2988–3002 (2026)
https://doi.org/10.1121/10.0046796

View Online
Export Citation

Connected Content

A companion article has been published: Improving how we steer and sense sound

Articles You May Be Interested In

Acoustic source localization based on acoustic leaky-wave antenna with heterogeneous structure

J. Acoust. Soc. Am. (January 2023)

Tunable local sensitivity in ultrasound waveguides via selective tapering: Newtonian viscosity sensing

Appl. Phys. Lett. (September 2026)

Feasibility of graphene CRLH metamaterial waveguides and leaky wave antennas

J. Appl. Phys. (July 2016)

30 October 2026 08:24:33

ASA
ACOUSTICAL SOCIETY OF AMERICA

ASA
LEARN MORE
Advance your science and career as a member of the
Acoustical Society of America

JASA ARTICLE

A quasi-uniform acoustic leaky-wave antenna: Analysis, design and experimental validation

Jens Forssén,[1,a] Pablo-Antonio Martínez-Vicente,[2] Astrid Algaba-Brazález,[2] Matthew Polidano,[1] and José-Luis Gómez-Tornero[2]

[1]*Division of Applied Acoustics, Department of Architecture and Civil Engineering, Chalmers University of Technology, SE-412 96 Gothenburg, Sweden*

[2]*Department of Communication and Information Technologies, Technical University of Cartagena, 30202 Cartagena, Spain*

ABSTRACT:

This paper introduces an efficient analytical tool for the design of quasi-uniform acoustic leaky-wave antennas (ALWAs) based on circular holes perforated along the broad wall of a rectangular acoustic waveguide, together with experimental validation in terms of frequency-scanning capability. The analytical formulation combines the transverse equivalent network and the transverse resonance equation to predict leaky-mode dispersion parameters, including the phase constant and leakage rate. Compared with previously reported metamaterial-based ALWAs, which rely on complex resonant unit cells and exhibit limited scanning performance, the proposed structure provides a simpler alternative while maintaining effective beam-steering capability. The proposed approach bridges the gap between theoretical modeling and practical implementation, establishing a robust framework for the design and optimization of compact and cost-effective ALWAs suitable for acoustic sensing, communication, and localization applications.

© *2026 Author(s). All article content, except where otherwise noted, is licensed under a Creative Commons Attribution (CC BY) license (https://creativecommons.org/licenses/by/4.0/).* https://doi.org/10.1121/10.0046796

(Received 6 March 2026; revised 13 September 2026; accepted 14 September 2026; published online 13 October 2026)

[Editor: Thomas Edward Blanford] Pages: 2988–3002

30 October 2026 08:24:33

I. INTRODUCTION

Leaky-wave antennas (LWAs)[1–3] have been extensively investigated in the electromagnetic (EM) domain as progressive-wave structures capable of generating directive radiation patterns with simple feeding (source) arrangements and frequency-dependent beam scanning. Initially developed for microwave and radio frequency applications, they were later extended to optics, where similar dispersive mechanisms enabled beam steering in integrated waveguides.[4] More recently, these principles have been adapted to acoustics, giving rise to acoustic leaky-wave antennas (ALWAs), which transform frequency variations into controlled spatial beam scanning and enable direction finding without the need for complex phased arrays.[5–8] This property makes them attractive for scenarios where compactness, low cost, sustainability, and reduced hardware complexity are essential, since they enable angular estimation with a single microphone/loudspeaker rather than typical multi-element microphone/loudspeaker arrays, minimizing the number of transmit/receive (Tx/Rx) electronics.

Compared to traditional acoustic transducer arrays (microphone/loudspeaker arrays), which require multiple synchronized elements and complex control electronics, ALWAs can provide angular selectivity using a single excitation source and receiver. This results in significantly simpler, lighter, and more cost-effective architectures suitable for acoustic direction finding, source localization, and communication systems.[9–11] Their ability to perform frequency-to-angle mapping enables direct estimation of the direction of arrival with a single microphone when combined with appropriate signal-processing algorithms, as previously demonstrated in EM LWAs for localization and sensing.[12–14] These attributes make ALWAs particularly attractive for resource-constrained scenarios such as robotic navigation, structural monitoring, and autonomous sensing in the Internet of Things (IoT). Recently, the use of acoustic localization of WiFi devices has been experimentally demonstrated.[15] In addition, ALWAs have also been proposed as acoustic dispersive prisms, devices capable of separating different frequency components of a broadband signal into distinct angular directions,[9] opening perspectives for applications in spectral analysis and acoustic imaging.

Several types of ALWAs have been reported, demonstrating different approaches to achieve acoustic beam steering, mainly based on acoustic metamaterials. In particular, some designs introduced periodic metamaterial-based unit cells incorporating resonant inclusions such as membranes or Helmholtz resonators to engineer the structure's dispersion, thereby controlling the beam direction as a function of frequency and, in some cases, achieving composite right/left-handed (CRLH) behavior.[10,16–18] These configurations enable backward-to-forward beam scanning across wide angular sectors.

Despite these advances, periodic and metamaterial-based ALWAs still face significant challenges such as manufacturing complexity, strong viscothermal losses, and

[a]Email: jens.forssen@chalmers.se

 ©Author(s) 2026.

https://doi.org/10.1121/10.0046796

narrow operating bandwidths, which limit their experimental performance and practical applicability.[19] Moreover, many prototypes have shown restricted scanning ranges and have failed to demonstrate consistent radiation across the full predicted angular span.[16,20] For example, a metamaterial-based ALWA employing a cylindrical waveguide with periodic modifications was numerically proposed in Ref. 20, but its experimental validation of the proof-of-concept was not fully demonstrated. The lack of proper laboratory settings, including an acoustic anechoic chamber, may have reduced the reliability of the reported radiation patterns. Furthermore, only a limited set of measurement angles was recorded, preventing a clear reconstruction of the beam shape and sidelobe levels, thus limiting the evidence for frequency-scanning performance in spatial localization tasks. Consequently, although simulations often predict broadband scanning, the experimental evidence of ALWAs has so far remained inconclusive.

Recent efforts have attempted to address the challenges of practical ALWA implementations (complex configurations, narrow beam-scanning angles, limited bandwidth, manufacturing difficulties, etc.) by introducing heterogeneous loading strategies, where the acoustic impedance is spatially varied along the waveguide to improve directivity and scanning range.[8] However, most of these approaches still rely on periodic or complex metamaterial configurations whose analytical treatment is computationally demanding. The analysis of metamaterial-based ALWAs is typically performed using full-wave numerical simulations such as the finite element method (FEM),[21] which, although accurate, is computationally intensive and unsuitable for iterative design.

Alternatively, uniform and quasi-uniform ALWAs, in which acoustic leakage is achieved through non-resonant apertures such as slits or holes, offer a simpler and more scalable solution than metamaterial-based counterparts. An antenna with identical perforations spaced at a constant distance much shorter than the wavelength behaves like a uniform antenna and is said to be quasi-uniform, as explained in another study.[2] This type of antenna has been extensively investigated in the EM domain, where also the introduction of gradual variations along the aperture geometry through slits[1,22] or holes[23,24] enables improved control of both the leakage rate and beam scanning direction. Although conceptually simple, their theoretical and experimental study in acoustics remains limited and has not been explored in detail in the literature. Analytical formulations based on the transverse equivalent network (TEN) and transverse resonance equation (TRE), well established in the EM domain,[22,25–28] provide a highly efficient alternative to full-wave simulation. These techniques capture the key physical behavior of leaky modes using compact circuit-based representations, drastically reducing computational cost. Extending such methods to the acoustic field can therefore enable faster and more accurate design methodologies for uniform and quasi-uniform ALWAs.

In this work, a quasi-uniform ALWA is theoretically analyzed, designed, and experimentally validated. The proposed structure consists of a rectangular acoustic waveguide with an array of circular perforations along its broad wall, acting as controlled leakage points. For the first time in acoustics, an analytical framework based on the TEN and TRE methods is developed and applied to a quasi-uniform ALWA to predict its leaky-mode dispersion characteristics, including the phase constant (and consequent beam-scanning direction) and the leakage rate. The proposed model enables an efficient and physically insightful analysis of the complex leaky-mode behavior, providing results that agree closely with full-wave simulations obtained via finite-element modeling in COMSOL Multiphysics, as well as with experimental measurements.

The paper is organized as follows: Sec. II introduces the theoretical framework for acoustic LWAs, including the waveguide formulation and the TEN/TRE-based dispersion analysis used to predict the radiation angle and leakage rate. Section III describes the methodology adopted for the study, including the theoretical implementation, finite-element modeling, and the design of the experimental prototype and the measurement setup. Section IV presents the results obtained from theoretical predictions, numerical simulations, and experimental measurements, together with a comparison between them. Finally, Sec. V summarizes the main conclusions and discusses potential extensions toward more advanced acoustic LWA designs.

II. THEORY

A. Acoustic waveguides

The sound pressure in a rectangular acoustic waveguide open in the z-dimension and with rigid walls in the x and y-dimensions can be formulated as[29]

$$
\begin{aligned}
p_{nm} &= \sum_{n,m} A_{nm}\cos(k_{xn}x)\cos(k_{ym}y)e^{j(\omega t - k_z z)} \\
k_0^2 &= k_{xn}^2 + k_{ym}^2 + k_z^2, \qquad k_0 = \frac{\omega}{c} \\
k_z &= \left[\left(\frac{\omega}{c}\right)^2 - \left(k_{xn}^2 + k_{ym}^2\right)\right]^{1/2} \\
k_{xn} &= \frac{n\pi}{W}, \qquad n = 0, 1, 2, \ldots \\
k_{ym} &= \frac{m\pi}{H}, \qquad m = 0, 1, 2, \ldots.
\end{aligned} \tag{1}
$$

Here, A_{nm} is the amplitude of the mode (n,m), W and H are the lengths of the cavity in dimensions x and y, respectively, t is time, ω is the angular frequency, c is the sound speed, and k_{xn} and k_{ym} represent the wavenumbers for the axis and mode specified by the subscript. Here, it is assumed that the source is located at $z = 0$ and that the acoustic energy propagates in the positive z-direction.

If $k_0^2 = (\omega/c)^2$ is larger than $k_{xn}^2 + k_{ym}^2$, the value of k_z is real and there is propagation in the positive z-direction. If, on the other hand, k_0^2 is smaller than $k_{xn}^2 + k_{ym}^2$, the value of k_z is imaginary, corresponding to an exponentially decaying

30 October 2026 08:24:33

field along the z-axis. The transition is the cutoff frequency of mode (n,m), given by[29]

$$\omega_{nm} = ck_{nm} = c\sqrt{k_{xn}^2 + k_{ym}^2}. \tag{2}$$

If the waveguide is excited at a certain driving frequency, all modes with a cutoff frequency below the driving frequency may propagate in the waveguide, whereas all modes with a cutoff frequency higher than the driving frequency will decay exponentially.[29] In the following, we will assume that the height of the waveguide, H, is sufficiently small such that the working frequency range of interest will only allow propagating modes with $m = 0$, i.e., the wavenumber in the y-direction is zero.

B. Quasi-uniform leaky wave antenna

Introducing perforations, or other impedance changes, on the waveguide wall at $x = W$ allows radiation to the outside, for which the pressure field can be written as[10,20]

$$p(x,z) = p_0 e^{-jk_x x} e^{-jk_z z}, \tag{3}$$

where the propagation angle is shown in Fig. 1. It is assumed that the perforations are densely spaced in comparison to the acoustic wavelength whereby a uniform impedance can be assumed, modeled as an effective impedance, i.e., a quasi-uniform LWA.

The wavenumber k_z will generally be complex and can be written as $k_z = \beta - j\alpha$,[20] where the leakage factor α and the propagation constant β are the two fundamental parameters for the design of an ALWA.[30] For $|\beta|$ smaller than k_0, the real part of k_x becomes larger than zero, and radiation occurs,[10,30] i.e., we have an ALWA.

C. Radiation angle and leakage factor

The propagation constant, β, determines the angle of radiation, given by[10,20,30]

$$\theta = \sin^{-1}\left(\frac{\beta}{k_0}\right). \tag{4}$$

The leakage factor, α, determines the amount of radiation per unit length,[30] assuming that other losses are negligible, e.g., those due to viscous friction at openings. Assuming a reflection-free termination at the end of the antenna, the leakage factor can be calculated from[10]

$$\Psi_2 = \Psi_1 e^{-2\alpha l_{12}}, \tag{5}$$

where Ψ_1 and Ψ_2 are the powers through an interior cross section of the antenna at two locations separated by a distance l_{12}, which gives

$$\alpha = \frac{1}{2l_{12}} \ln\left(\frac{\Psi_1}{\Psi_2}\right). \tag{6}$$

The radiated power is associated with the active part of the leakage factor and is given by the real part of the complex-valued power. The reactive power is not contributing to the leaky-wave radiation but is associated with power that is reflected back to the source.[31,32] The instantaneous acoustic power in a cross section of the antenna cavity can be calculated for a single-frequency sound field as[33]

$$\Psi = \int_S \mathbf{I}_c \cdot \hat{\mathbf{z}}\, dS, \tag{7}$$

$$\mathbf{I}_c = \frac{1}{2} p \mathbf{u}^*, \tag{8}$$

where S is the area of the cross section of the antenna parallel to the xy-plane, $\hat{\mathbf{z}}$ is the unit vector in the z-direction, $\mathbf{I}_c(x,y)$ is the instantaneous complex intensity, p is the complex pressure, $\mathbf{u}$ is the complex particle velocity, and * denotes the complex conjugate. Using the specific acoustic impedance, defined as the ratio of pressure and particle velocity, $Z^s_{0,z} = p/\mathbf{u} \cdot \hat{\mathbf{z}}$, with $Z^s_{0,z} = \rho_0\omega/k_z$, where ρ_0 is the air density, we get

$$\mathbf{u}^* \cdot \hat{\mathbf{z}} = \frac{p^* k_z^*}{\rho_0 \omega}. \tag{9}$$

Using $k_z^* = \beta + j\alpha$ and Eqs. (7)–(9), the instantaneous power at the source can be calculated as

$$\Psi(0) = \frac{(\beta + j\alpha)}{2\rho_0\omega} \int_S |p|^2\, dS. \tag{10}$$

From Eq. (5), the power at distance z from the source can be expressed as

$$\Psi(z) = \Psi(0) e^{-2\alpha z}. \tag{11}$$

The leakage factor can be found through differentiation of the power expression in Eq. (11) with respect to z,[32]

$$-\frac{d\Psi(z)}{dz} = 2\alpha\Psi(0) e^{-2\alpha z}, \tag{12}$$

i.e.,

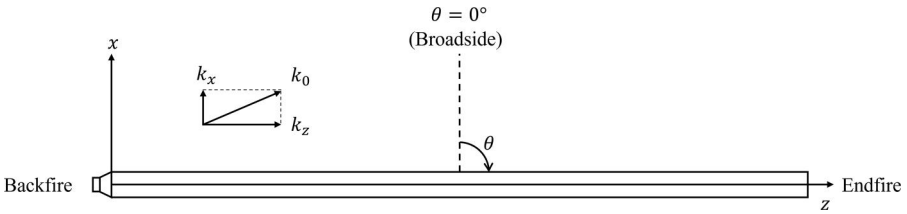

FIG. 1. Defining the directions for the ALWA.

30 October 2026 08:24:33

https://doi.org/10.1121/10.0046796

$$-\frac{\mathrm{d}\Psi(z)}{\mathrm{d}z} = 2\alpha\Psi(z). \tag{13}$$

Upon studying the real part of this, the active component of α can be identified as[31]

$$\alpha_{\text{active}} = \frac{\mathrm{Re}\left[-\frac{\mathrm{d}\Psi(z)}{\mathrm{d}z}\right]}{2|\Psi(z)|}, \tag{14}$$

which can also be written as

$$\alpha_{\text{active}} = \alpha\frac{\beta}{\sqrt{\alpha^2+\beta^2}}. \tag{15}$$

The corresponding formulation for the reactive part can be written as

$$\alpha_{\text{reactive}} = \alpha\frac{\alpha}{\sqrt{\alpha^2+\beta^2}}, \tag{16}$$

such that $\alpha^2_{\text{active}} + \alpha^2_{\text{reactive}} = \alpha^2$ is fulfilled. In the results from the theoretical solution, we will, due to convention, plot the total leakage factor,

$$\alpha = \frac{\left|\frac{\mathrm{d}\Psi(z)}{\mathrm{d}z}\right|}{2|\Psi(z)|}. \tag{17}$$

D. Design parameters of an ALWA

A simple design of a uniform ALWA is a rectangular waveguide with a slit-perforation on one side. Here, a series of circular holes is used instead of a slit, making the antenna fulfill a quasi-uniform design provided that the periodic spacing is much smaller than the wavelength. The geometry of such an ALWA design is shown in Fig. 2, where the propagation inside the antenna is in the z-direction, perpendicular to the xy-plane. The source is located at one end of the ALWA ($z = 0$), and at the opposite end ($z = L$), a reflection-free termination is assumed. The length of the ALWA, L, needs to be significantly larger than the wavelength of the lowest operating frequency.

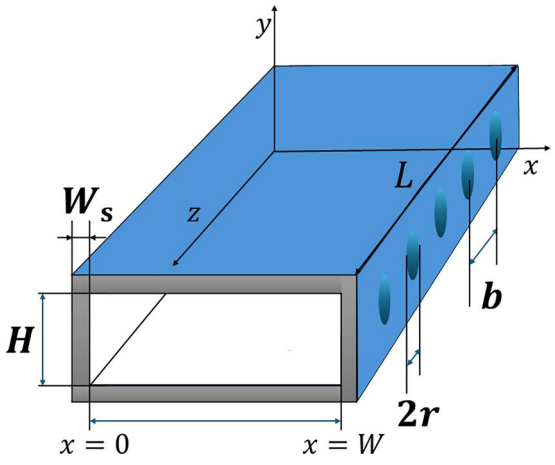

FIG. 2. Geometry of the ALWA.

The pressure of the sound waves in the x-direction of the ALWA can be modeled as a linear combination of waves, formulated as[29]

$$p(x,t) = Ae^{j[\omega t + k_x(W-x)]} + Be^{j[\omega t - k_x(W-x)]} \tag{18}$$

where A and B are the amplitudes of the forward and backward traveling waves, respectively. To find a relation between A and B, the boundary conditions for pressure and particle velocity are used. The relation between particle velocity and pressure is given by[29]

$$u(x,t) = -\frac{1}{\rho_0}\int\frac{\partial p}{\partial x}\,dt, \tag{19}$$

which gives

$$u(x,t) = -\frac{1}{j\omega\rho_0}\cdot\frac{\partial p}{\partial x}. \tag{20}$$

Inserting this into Eq. (18) gives

$$u(x,t) = \frac{1}{\omega\rho_0}\left[Ak_xe^{jk_x(W-x)} - Bk_xe^{-jk_x(W-x)}\right]e^{j\omega t}. \tag{21}$$

Using the impedances at the left and right walls, $Z_L = p(0,t)/u(0,t)$ and $Z_R = p(W,t)/u(W,t)$, respectively, we can write

$$Z_L = \frac{\omega\rho_0}{k_x}\cdot\frac{(Ae^{jk_xW} + Be^{-jk_xW})}{(Ae^{jk_xW} - Be^{-jk_xW})} \quad \text{at } x = 0, \tag{22}$$

$$Z_R = \frac{\omega\rho_0}{k_x}\cdot\frac{(A+B)}{(A-B)} \quad \text{at } x = W. \tag{23}$$

With $Z_{0,x} = \rho_0\omega/k_x$, the characteristic impedance of the ALWA in the x-direction, we get,

$$Z_R = Z_{0,x}\cdot\frac{A+B}{A-B}, \tag{24}$$

which, inserted in Eq. (23), gives

$$A = B\cdot\frac{Z_R + Z_{0,x}}{Z_R - Z_{0,x}}. \tag{25}$$

Using Eq. (25) in Eq. (22) results in

$$Z_L = Z_{0,x}\cdot\frac{B\frac{Z_R+Z_{0,x}}{Z_L-Z_{0,x}}e^{jk_xW} + Be^{-jk_xW}}{B\frac{Z_R+Z_{0,x}}{Z_L-Z_{0,x}}e^{jk_xW} - Be^{-jk_xW}}, \tag{26}$$

which can be simplified to

$$Z_L = \frac{Z_R + jZ_{0,x}\tan(k_xW)}{1 + j\frac{Z_R}{Z_{0,x}}\tan(k_xW)}. \tag{27}$$

30 October 2026 08:24:33

If the wall at $x = 0$ is rigid, the boundary condition must meet $u(0,t) = 0$, i.e.,

$$k_x(Ae^{jk_xW} - Be^{-jk_xW}) = 0, \tag{28}$$

which gives

$$A = Be^{-2jk_xW}. \tag{29}$$

Insertion of Eq. (29) into Eq. (23) results in

$$Z_R = Z_{0,x} \cdot \frac{e^{-jk_xW} + e^{jk_xW}}{e^{-jk_xW} - e^{jk_xW}}, \tag{30}$$

which equates to

$$Z_R = -jZ_{0,x}\cot(k_xW). \tag{31}$$

Solving for k_x gives

$$k_x = \frac{1}{W} \cdot \left[\arctan\left(j\frac{Z_{0,x}}{Z_R}\right) + n\pi\right], \quad n = 0, 1, 2, \ldots \tag{32}$$

Equation (32) for k_x is similar to the case of the closed waveguide, but contains an additional term $\arctan(jZ_{0,x}/Z_R)$, due to the influence of the finite impedance wall. This additional term allows for a non-zero value of k_x for the case where $n = 0$, and hence this allows for leaky-wave radiation for the (0,0) mode.

In the following, the (0,0) and (1,0) modes are studied. Since the impedances in Eq. (32) depend on k_x, the equation does not represent a closed-form solution. How to solve for k_x, and to find k_z, will be treated in Sec. II G.

E. Predicting the mode shapes

The mode-shape, i.e., the shape of the pressure pattern in the cross section of the antenna, can be found by substituting the expression found for A in Eq. (29) into Eq. (18). Including also the dependence in the y-direction, from Eq. (1), the resulting equation for the pressure mode (n,m) is

$$\begin{aligned} p_{n,m}(x,y) &= B\left(e^{-jk_{x,n}(W+x)} + e^{-jk_{x,n}(W-x)}\right)\cos(k_{y,m}y) \\ &= A_{nm}e^{-jk_{x,n}W}\cos(k_{x,n}x)\cos\left(\frac{m\pi}{H}y\right), \end{aligned} \tag{33}$$

where $k_{x,n}$ and $k_{y,m}$ denote k_x and k_y evaluated for mode (n,m) and A_{nm} is the amplitude of mode (n,m). The total pressure is given by the sum of all the modes excited in the waveguide, i.e.,

$$\begin{aligned} p(x,y) = &\sum_{n,m} A_{nm}e^{-jk_{x,n}W} \\ &\times \cos\left\{\left[\arctan\left(j\frac{Z_{0,x}}{Z_R}\right) + n\pi\right]\frac{x}{W}\right\}\cos\left(\frac{m\pi}{H}y\right), \end{aligned} \tag{34}$$

where k_x from Eq. (32) has been inserted. In Fig. 3, the modes $(0,0)$ and $(1,0)$ are plotted as a function of x using

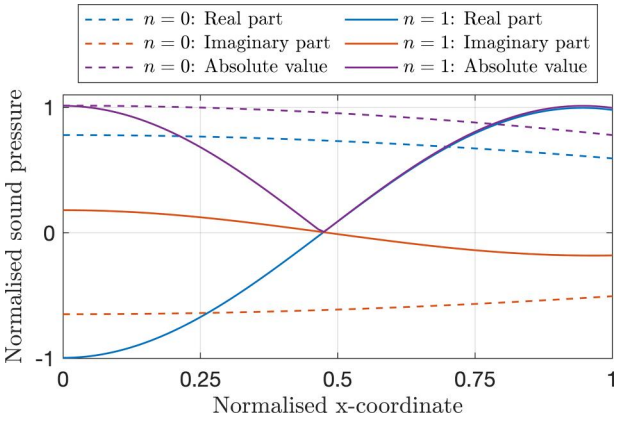

FIG. 3. Mode shapes for $n = 0$ and $n = 1$ exemplified for the antenna with circular perforations.

Eq. (33) with $f = 400\,\text{Hz}$ for $n = 0$ and $f = 1900\,\text{Hz}$ for $n = 1$, and normalizing by setting $A_{nm}\exp(-jk_{x,n}W) = 1$. The impedance model for Z_R is described in Sec. II F. For the $n = 1$ mode, it is interesting to note that the zero-crossing of the real part is not centered along the x-direction. This observation suggests that the excitation location could be optimized.

F. Modeling the impedance for periodically spaced holes

The surface impedance of a circular hole is given by[34]

$$Z_S = j\omega\rho_e l, \quad \rho_e = \rho_0\left[1 - \frac{2}{s\sqrt{-j}}\frac{J_1(s\sqrt{-j})}{J_0(s\sqrt{-j})}\right]^{-1}, \tag{35}$$

where l is the neck-length of the cylindrical hole (i.e., W_S in Fig. 2) and $s = r\sqrt{\omega\rho_0/\mu}$, where r is the radius of the hole and μ is the coefficient of viscosity of air, which provides friction losses.

The radiation impedance of a circular hole at the end of a long tube for values of $kr < 0.5$ can be approximated as:[35]

$$Z_{11} = \frac{1}{4}\rho_0 c k_0^2 r^2 + 0.6134 j\rho_0 c_0 k_0 r. \tag{36}$$

The impedance at the end of a tube was chosen because for low frequencies, the baffle formed by the antenna is small compared to the wavelength and behaves similarly to a long tube. Furthermore, to account for both ends of the hole, the imaginary part of Z_{11} is multiplied by two.[36]

To obtain the specific impedance of the linear array of circular holes, it must be normalized by the porosity, ϕ.[36] This can be calculated as the ratio of the area of a single hole to the area of the surface corresponding to that hole, i.e.,

$$\phi = \frac{\pi r^2}{bH}, \tag{37}$$

where b is the hole separation and H is the height of the ALWA cavity as shown in Fig. 2.

30 October 2026 08:24:33

https://doi.org/10.1121/10.0046796

Furthermore, the mutual impedance of adjacent holes should be considered. The mutual impedance of two identical holes with the same phase and amplitude is given by[37]

$$Z_{12} = R_{11}\left[\frac{\sin kb}{kb} + j\frac{\cos kb}{kb}\right], \tag{38}$$

where R_{11} is the real part of the radiation impedance of a single hole and k is the wavenumber. Considering a single hole with N holes on either side with a hole spacing of b, the total impedance for this hole would be

$$Z_r = Z_{11} + 2\cdot\sum_{n=1}^{N} R_{11}\left[\frac{\sin nkb}{nkb} + j\frac{\cos nkb}{nkb}\right]. \tag{39}$$

To simplify the mutual-coupling model, only the two nearest neighboring perforations on each side of the reference hole are included [see Eq. (40)]. Additional analytical calculations considering larger numbers of neighboring holes showed only minor changes in the predicted leakage rate and negligible differences in the radiation angle, with the solution rapidly converging as the number of neighbors increases. Physically, the influence of distant perforations decreases because the phase difference between holes increases with distance. Therefore, considering only the nearest neighbors provides an accurate approximation for the antenna investigated in this work. Hence, the total impedance is modeled as

$$\begin{aligned} Z_R = {} & \frac{j\omega\rho_0 l}{\phi}\left[1 - \frac{2}{s\sqrt{-j}}\frac{J_1(s\sqrt{-j})}{J_0(s\sqrt{-j})}\right]^{-1} \\ & + \frac{\rho_0 c (k_0 r)^2}{4\phi}\left[1 + 2\cdot\sum_{n=1}^{2}\left(\frac{\sin nkb}{nkb} + j\frac{\cos nkb}{nkb}\right)\right] \\ & + 2\times 0.6134 j\frac{\rho_0 c}{\phi}kr. \end{aligned} \tag{40}$$

G. TEN/TRE formulation for leaky-mode dispersion

For the design of a LWA, it is useful to analyze the guided-mode propagation through the transverse cross section of the waveguide. To this end, we use the TEN, which represents the waveguide cross section as an equivalent circuit model (see Fig. 4), thereby reducing the original three-dimensional (3D) guided-wave problem to a one-dimensional (1D) transverse formulation. This approach makes it possible to efficiently determine suitable values of the design parameters in order to control the leakage rate and the frequency dependence of the scanning angle.

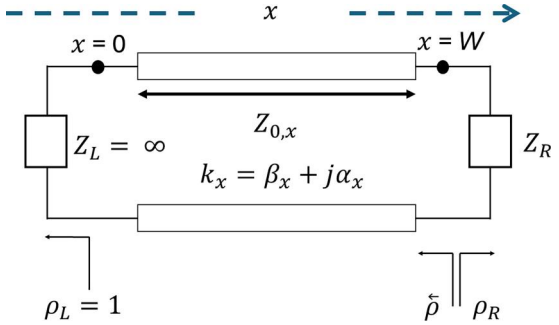

FIG. 4. General TEN model of the cross section for a rectangular acoustic waveguide with a lateral opening perturbation.

The circuit topology in Fig. 4 is inherited from the EM TEN/TRE formulation used for LWAs, where the transverse field problem is mapped onto an equivalent transmission line section of length W with a characteristic impedance $Z_{0,x}$. In that EM interpretation, the two long parallel lines in Fig. 4 correspond to the two conductors of the transmission-line representation, and the terminal loads Z_L and Z_R implement the boundary conditions through equivalent impedances (e.g., modeling the lateral guide walls and the openings).[38] Here, we use the same formalism in acoustics by working with the pressure/volume velocity variables ($Z = p/U$). Under this framework, the right-hand side with the openings can be represented by an equivalent acoustic impedance Z_R that models the wall with radiating surface openings where the mode leaks into the exterior air. The left-hand side here models an acoustically hard surface with infinite impedance.

The equivalent network shown in Fig. 4 should be interpreted as an equivalent representation of the acoustic waveguide cross section rather than as an electrical circuit. Its purpose is not merely to analyze the acoustic field, but to provide a compact analytical framework for antenna design. By representing the acoustic boundary conditions through equivalent impedances, the transverse resonance condition can be formulated in a simple manner, allowing the propagation constant, beam-scanning angle and leakage rate to be efficiently predicted without repeated full-wave numerical simulations.

Unlike Bloch-based formulations used by Bongard *et al.*,[39] which determine the propagation characteristics by analyzing the longitudinal periodicity of the structure, the proposed TEN/TRE approach analyzes the transverse cross section of the waveguide. The perforated wall is represented by an equivalent acoustic radiation impedance, allowing the propagation constant to be obtained from the transverse resonance condition. Consequently, the proposed formulation is naturally applicable to both uniform and quasi-uniform ALWAs, whereas Bloch-based approaches are primarily intended for periodic structures.

To analyze the TEN, a resonance condition is imposed on the reflection factors, yielding the TRE in terms of the reflection coefficients,[24,25]

$$\overleftarrow{\rho}\cdot\rho_R = 1. \tag{41}$$

Here, ρ_R is the complex reflection factor of the opening surface

$$\rho_R = |\rho_R| e^{j\psi_R} = \frac{Z_R - Z_{0,x}}{Z_R + Z_{0,x}}, \tag{42}$$

and $\overleftarrow{\rho}$ is the effective reflection factor seen when looking from the opening toward the opposite side

30 October 2026 08:24:33

$$\overleftarrow{\rho} = \rho_L e^{-j2k_x W}, \tag{43}$$

where ρ_L denotes the reflection factor at the left wall, which is modeled as a rigid boundary condition, i.e., $\rho_L = 1$.

The complex exponential term in Eq. (43) represents the phase accumulated during the one-way and return across the transmission line. Substituting Eqs. (42) and (43) into Eq. (41), we get, with $k_x = \beta_x + j\alpha_x$,

$$|\rho_R| e^{j\psi_R} \cdot e^{-j2\beta_x W} \cdot e^{2\alpha_x W} = 1. \tag{44}$$

Rearranging terms leads to

$$e^{-j2\beta_x W} \cdot e^{2\alpha_x W} = \frac{1}{|\rho_R|} e^{-j\psi_R}. \tag{45}$$

This complex equation is satisfied by independently enforcing the phase and magnitude conditions. First, the phase condition requires,

$$2\beta_x W = \psi_R + 2\pi n, \qquad n \in \mathbb{N}, \tag{46}$$

where n is the transverse mode index arising from the 2π phase ambiguity of the resonance condition; each step in n selects a higher-order transverse mode branch, which becomes propagating as the operating frequency increases above cutoff. This gives

$$\beta_x = \frac{\psi_R + 2\pi n}{2W}. \tag{47}$$

Second, the magnitude condition gives

$$\alpha_x = \frac{1}{2W} \ln\left(\frac{1}{|\rho_R|}\right). \tag{48}$$

Combining real and imaginary parts, the transverse wavenumber can be expressed as

$$k_x = \beta_x + j\alpha_x = \frac{\psi_R + 2\pi n}{2W} + j\frac{1}{2W} \ln\left(\frac{1}{|\rho_R|}\right). \tag{49}$$

From before, we conclude that given an impedance model for the aperture surface, the transverse wavenumber can be determined.

Since ρ_R depends on the characteristic impedance [Eq. (42)], which depends on k_x, Eq. (49) becomes a transcendental equation of the form $k_x = F(k_x)$, which does not admit a closed-form solution. To solve for k_x, we define an objective function $M(k_x)$ to be numerically minimized,

$$M(k_x) = |k_x - F(k_x)|, \tag{50}$$

where $F(k_x)$ is the transcendental function obtained from Eq. (49),

$$F(k_x) = \frac{\psi_R(k_x) + 2\pi n}{2W} + j\frac{1}{2W} \ln\left(\frac{1}{|\rho_R(k_x)|}\right). \tag{51}$$

Since $M(k_x)$ may exhibit multiple local minima, optimization is initialized with an analytical estimate of k_x, obtained by evaluating Eq. (49) with the plane wave characteristic impedance $Z_0 = \omega\rho_0/k_0$, which makes ρ_R independent of k_x in Eq. (42) and provides a robust starting point. Once the transverse wavenumber k_x is obtained from the numerical solution of the TRE, the associated complex longitudinal wavenumber k_z is given by $k_z = \sqrt{k_0^2 - k_x^2}$. Due to the assumption $H < \lambda/2$, the modes are taken to be invariant along the y direction, which implies $k_y = 0$.

We next recall the standard leaky-wave relations used to quantify the radiation performance of an ALWA. From the complex longitudinal wavenumber of the leaky mode,

$$k_z = \beta - j\alpha, \tag{52}$$

the phase constant β determines the main-beam scanning angle (measured from broadside), while the leakage rate α governs the longitudinal power decay. In particular, the beam direction can be approximated by,[24]

$$\theta(f) \approx \arcsin\left(\frac{\beta(f)}{k_0}\right), \tag{53}$$

and the half-power beam width of a uniformly excited effective aperture can be estimated as[24]

$$\Delta\theta \approx \lambda_0 \frac{57^\circ}{L} \frac{1}{\cos\theta}. \tag{54}$$

Using the previous solution, the radiation behavior of the ALWA is conveniently characterized by the frequency–beam scanning curve $\theta(f)$ together with the normalized leakage curve $\alpha(f)/k_0$. It should be noted that Eq. (53) is a general leaky-wave relation and is therefore not specific to the proposed TEN/TRE formulation. Regardless of the analytical approach adopted to determine the propagation constant, the radiation angle is governed by the same relationship between the phase constant of the guided mode and the free-space wavenumber. The difference between the various formulations lies in the procedure used to obtain the propagation constant, rather than in the radiation condition itself.

III. METHOD

A. Theoretical solution

A quasi-uniform ALWA with dimensions listed in Table I is studied using the proposed TRE method. The TEN, which applies the transverse resonance condition, is implemented in Matlab to solve Eq. (50) for k_x using the `fminsearch` function[40] to minimize the objective function $M(k_x)$. The resulting solution is then used to compute the radiation angle, θ, and the normalized leakage rate α/k_0.

A parametric study was performed varying the radius, r, and width, W. The resulting dispersion curves, which are obtained by varying a single design parameter at a time, the hole radius r or the waveguide width W, are reported in

30 October 2026 08:24:33

https://doi.org/10.1121/10.0046796

TABLE I. Geometric parameters of the prototype antenna used for validation.

Parameter	Value
H (ALWA cavity height)	35 mm
W (ALWA cavity width)	95 mm
L (ALWA length)	1.5 m
W_s (wall thickness)	2.5 mm
r (hole radius)	4 mm
b (hole separation)	30 mm

Figs. 5 and 6, respectively. Two modes are shown in both figures: the mode $n = 0$ which inherently exists and can propagate longitudinally without cutoff, and mode $n = 1$ which is analogous to the first higher-order transverse variation (referred to as the TE_{10} mode for rectangular EM waveguides).

We analyze the evolution of both modes in Fig. 5 as the hole radius approaches zero. As plotted in Fig. 5(a), mode $n = 0$ converges to the longitudinal closed-waveguide (CW) limit, yielding endfire radiation ($\theta = 90°$) across the entire frequency range, and a vanishing radiation leakage rate, as confirmed in Fig. 5(b). This is consistent with the fact that the mode $n = 0$ in a closed waveguide reduces to a plane wave with no leakage, propagating only along the z-axis and remaining uniform across the transverse direction. As the hole radius increases, the waveguide transitions to a leaky configuration, and the $n = 0$ mode becomes radiative. However, the scanning angle, θ, and the attenuation rate, α/k_0, change abruptly, indicating limited controllability of its radiation characteristics, as shown in both Figs. 5 and 6.

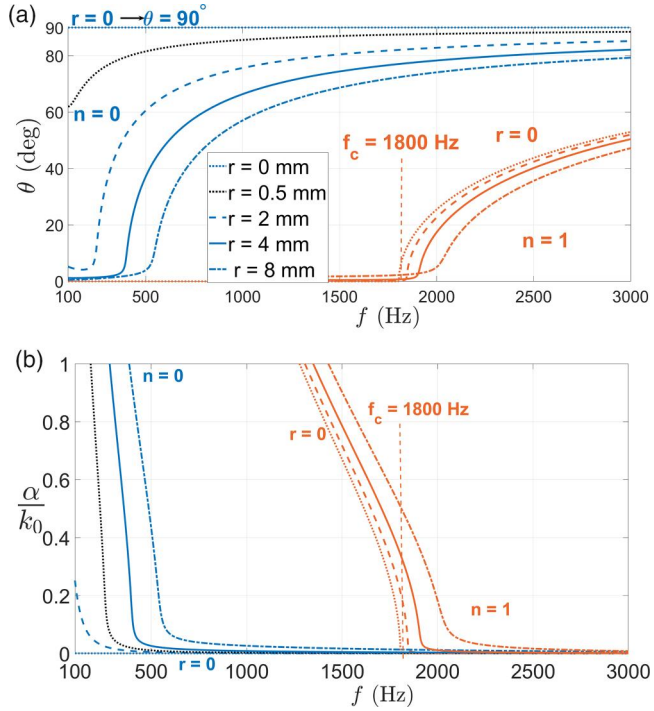

FIG. 5. Leaky-mode dispersion curves obtained for a quasi-uniform ALWA, as the aperture radius, r, varies. Including the CW limit ($r \to 0$).

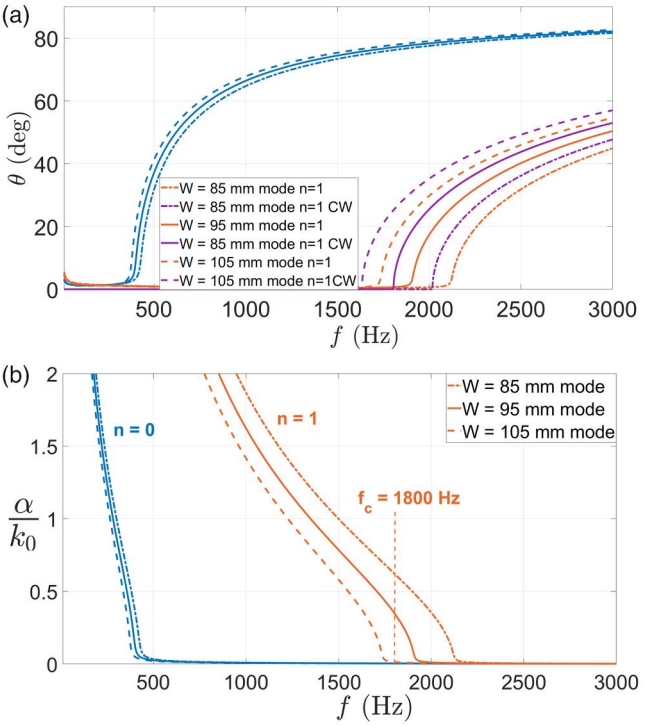

FIG. 6. Leaky-mode dispersion curves obtained for a quasi-uniform ALWA, as the width of the waveguide, W, varies.

In contrast, the mode $n = 1$ has an onset frequency around 1800 Hz, as seen in Figs. 5 and 6, consistent with the CW cutoff frequency of the higher-order mode in a conventional rectangular waveguide. For a very small hole radius (see Fig. 5), the solution for $n = 1$ approaches the CW limit. When the radius increases, so does the attenuation rate [Fig. 5(a)], as expected, but the mode preserves essentially the same dispersion curve, i.e., θ varies smoothly [Fig. 5(b)], in contrast to the mode $n = 0$, which exhibits an abrupt transition when the opening is introduced.

As shown in Fig. 6(a), as W increases, the dispersion curves are shifted in frequency, in a more pronounced way for the $n = 1$ mode than for the $n = 0$ mode. By comparing Figs. 5(a) and 6(a), it can be observed that the onset frequency of the angular scanning is more sensitive to changes in W than in r for $n = 1$. This behavior can be explained by the transverse resonance condition for $n = 1$, where the phase shift due to W is typically much larger than the phase shift due to ψ_R. This is further supported by Fig. 6(a), where the radiation curves of the $n = 1$ mode remain very close to those of the CW case, for which $\beta_x = \pi/W$. Thus, W mainly controls the transverse phase constant and the corresponding frequency shift, and therefore the scanning angle. Conversely, comparing Figs. 5(b) and 6(b), we can see that at a fixed frequency, the leakage rate is more sensitive to changes in r than in W. This provides a good mechanism for controlling α and θ by selecting r and W for a desired level of leakage and radiation angle, respectively.

An additional insight can be drawn from Fig. 6(a) by comparing the $n = 1$ scanning-angle curves with those for the CW condition. Only a slight frequency shift is observed

30 October 2026 08:24:33

compared to having openings, whereas the dispersion trend is practically preserved. This provides a useful tool for rapidly estimating the ALWA behavior using only the CW expression. In other words, a first-order prediction of θ can be obtained without solving the TRE and its associated transcendental equation. On the other hand, the closed waveguide approximation is not applicable to the mode $n = 0$, since in the closed case it reduces to a plane wave solution ($k_z \approx k_0$); consequently, the closed waveguide dispersion for $n = 0$ does not provide a meaningful reference to predict the open (leaky) behavior.

From these initial simulations, we conclude that the $n = 1$ leaky mode is more suitable for ALWA applications than the $n = 0$ leaky mode. For the $n = 1$ mode, the scanning angle, θ, and the normalized leakage rate, α/k_0, can be controlled smoothly by adjusting the radius, r, and the width of the waveguide, W, where r primarily controls leakage, while W controls beam scanning. This contrasts with the mode $n = 0$, which exhibits an abrupt transition from a closed mode to a leaky case, a characteristic that limits its practical controllability.

B. Finite element modeling

To validate the theoretical model, FEM calculations were carried out in COMSOL Multiphysics (version 6.2) using the *Pressure Acoustics, Frequency Domain* interface. The geometry was defined in COMSOL by creating the shape of the air inside the antenna and in a volume surrounding it, with the solid material of the ALWA assumed to be a perfectly rigid material. As the outer boundary, a sphere, truncated on the top, bottom, and backside to reduce computation time, was used (see Fig. 7). By trial and error, the minimum sphere size and degree of truncation were determined while maintaining negligible influence on the simulation results. Test calculations using a computational domain with twice the linear dimensions indicated a deviation of less than 1 dB within the radiation lobes. The outer boundary of the truncated sphere used the perfectly matched boundary (PMB) condition to suppress reflections.[41] These surfaces also enable External Field Calculation, used for extrapolating the sound field outside the model to compute far-field directivity.[42]

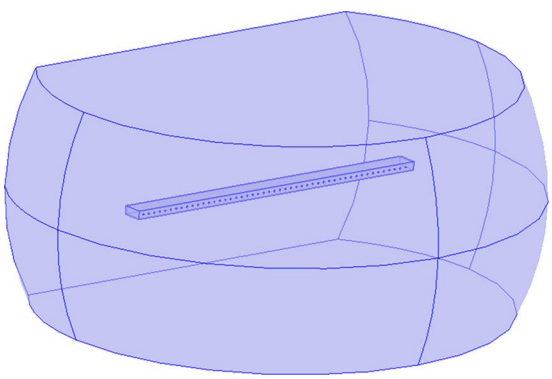

FIG. 7. COMSOL model showing the truncated sphere used as outer boundary in relation to the antenna (the outer boundary has a diameter of 2.4 m and a height of 1 m).

All ALWA walls except at the source and termination were treated as rigid, fully reflective boundaries.[43] The termination wall was given a PMB condition to model the ideal case of reflection-free termination. The influence of viscous friction was not included in the COMSOL model. Based on test calculations performed with the analytical model, both with and without viscous losses (results not shown), it was concluded that viscous losses can be neglected in the numerical study. Nevertheless, the influence of viscous losses remains of interest and calls for further investigation in future work.

For exciting the (0,0) mode in the ALWA, a velocity source condition was imposed on the whole interior of the source wall, with a chosen velocity amplitude of 0.1 m s^{-1}. To instead excite the (1,0) mode to a larger extent than the (0,0) mode, the interior source wall is split into two halves; one half with a velocity of 0.1 m s^{-1} and the other half with a velocity of -0.1 m s^{-1}. These two source settings simulate a theoretical monopole and dipole, respectively. Note that the numeric value of the amplitude can be chosen arbitrarily since it does not affect the final results in terms of radiation angle and leakage rate. The exterior of the source wall was modeled as rigid.

The mesh was constructed in COMSOL as free tetrahedral quadratic Lagrange elements with a frequency-varying size of 1/5 of the wavelength. This degree of refinement is generally considered sufficient and is also confirmed by comparing the results with the theoretical predictions. Modeling of viscous effects was not included here, which may need further mesh refinement.

The resulting sound pressure level directivity patterns were generated in COMSOL from the External Field Calculation and exported as a text file. Imported to MATLAB, the angle of the mainlobe was estimated by taking the maximum value of each directivity pattern, restricted to angles between 0° and 90° to avoid capturing the lobe on the back of the antenna.

The leakage rate estimate was based on power flows through cross-sectional planes of the ALWA cavity positioned close to the source and close to the termination. These quantities were inserted into Eq. (5), with the power flow at each plane obtained by surface integration of the active acoustic intensity output from Comsol.

C. Prototype construction and experimental setup

1. Manufacturing the ALWA

The ALWA was manufactured from a rectangular aluminum tube with dimensions listed in Table I. The dimensions were chosen to mainly prioritize good measurement quality for the (1,0) mode with a cutoff frequency estimated at 1800 Hz and the onset of the frequency-scanning behavior being around 1900 Hz [see Fig. 6(a)].

To make the ALWA operate in radiating mode, two loudspeaker elements were used as acoustic sources. A plastic

30 October 2026 08:24:33

https://doi.org/10.1121/10.0046796

fixture for the loudspeakers was 3D-printed (see Fig. 8) to be attached to the source end of the tube and sealed with tape.

To approximate a reflection-free termination, a 50 mm sample of mineral wool was placed inside the end of the tube. The estimated absorption of the mineral wool is about 130 dB/m at 1800 Hz and increases with frequency, whereby the reflection would be reduced by at least 13 dB at the frequency of the scanning onset and above. In future measurements, the absorption could be increased for further reduced reflections. To approximate a fully reflecting termination, a cut aluminum plate was attached to the end of the tube and sealed with tape.

2. Measurement method

The measurements were made in an anechoic chamber with an external control room. A measurement computer supplied the output signal to the loudspeakers (Visaton BF 32 S WP; Visaton, Haan, Germany), via a power amplifier (Fosi Audio ZA3; Fosi Audio, Shenzhen, China), and received the signals from two measurement microphones (GRAS 46AF; GRAS, Holte, Denmark) via a microphone amplifier (GRAS Power Module type 12AA). A loop-back connection was made from the output of the audio interface to an input channel, enabling a direct measurement of the loudspeaker's input signal.

The power amplifier was used in mono mode and connected to an in-house-built phase switch inside the anechoic chamber, which provides two output signals for two loudspeakers. Using the *monopole* setting of the switch, both loudspeakers are fed with the same signal in phase, whereas using the *dipole* setting, one of the loudspeakers is fed with the original input signal while a phase difference of 180° is applied to the other.

The antenna was placed on a rotating table (Varisphear) in an anechoic chamber, as shown in Figs. 9 and 10. A MATLAB program on the measurement computer was used to control the rotation in steps of 1° and to perform an impulse response measurement at each angle using the swept-sine technique (e.g., Ref. 44). An FFT was performed on the measured impulse response at each angle to obtain the directivity of the antenna through the magnitude of the frequency response function.



FIG. 8. Loudspeakers and loudspeaker fixture.

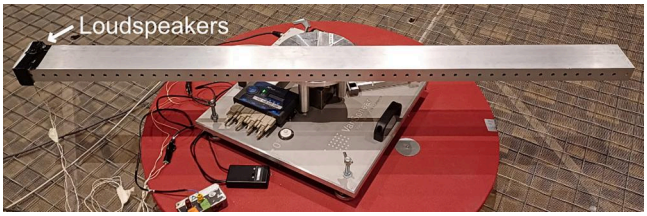

FIG. 9. The prototype antenna with attached loudspeakers, placed on the turntable.

Measurement data were collected using two microphones positioned 3–5 m from the center of the antenna. The measurements were performed twice, yielding four measurement values that were averaged to obtain the reported mean value. The measurement procedure was repeated for all four combinations of termination (absorber or reflector) and source type (monopole or dipole).

The measured directivities were used to determine the radiation angle by finding the angle of the maximum magnitude in the same way as for the Comsol simulation results.

When the measurements are performed with the reflector termination, a strong backward lobe is created as a counterpart to the main forward lobe. The difference in sound pressure level between the two lobes, $\Delta L_p = L_{p,\text{Forward}} - L_{p,\text{Backward}}$ (dB), is assumed to be determined by the interior power lost along the length, L, of the antenna,[45] i.e., $\Delta L_W = 10\log_{10}[\exp(2\alpha L)]$ (dB). Solving for α gives

$$\alpha = \frac{\Delta L_p}{20L\log_{10}\mathrm{e}}. \tag{55}$$

The radiation angle and leakage rate obtained from each microphone position were averaged, and the uncertainty of the mean values in terms of a 95% confidence interval is estimated as $u = ts/\sqrt{n}$ where s is the experimental standard deviation, n is the number of measurements, and t is determined from Student's t-distribution; $t = 3.18$

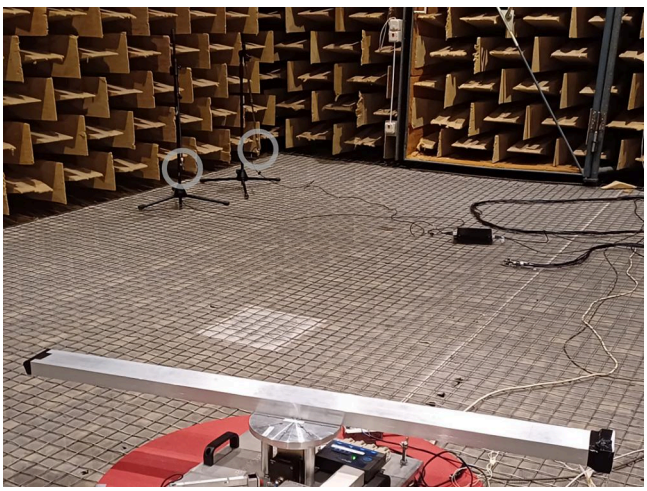

FIG. 10. The prototype antenna in the anechoic chamber. The measurement microphones are marked by gray circles.

30 October 2026 08:24:33

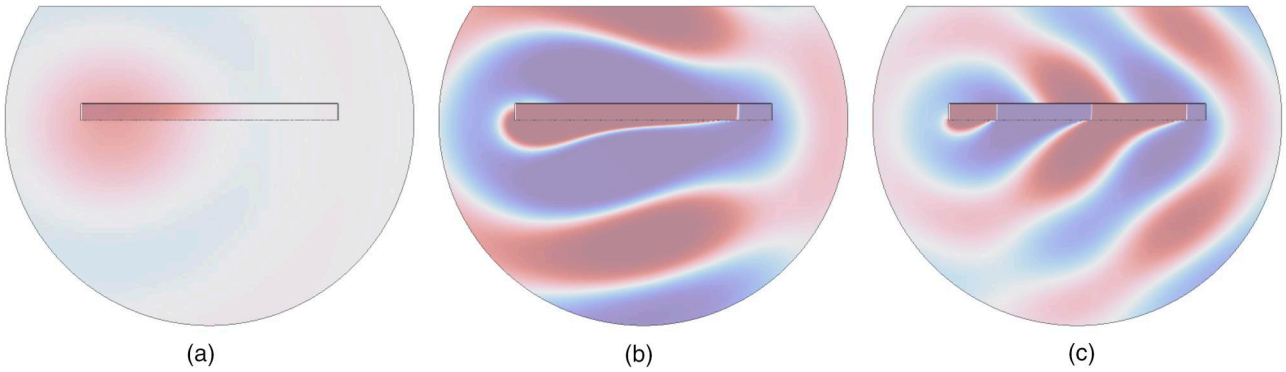

FIG. 11. Plots of the acoustic pressure amplitude (real part) for the antenna operated with a monopole source.

for $n = 4$ and 95% confidence interval. The uncertainty of the initial angle of the antenna was estimated to be about 2°.

IV. RESULTS

A. Resulting pressure fields from finite-element modeling

Calculations using finite-element modeling in COMSOL were carried out for both monopole and dipole excitations to study the (0,0) and the (1,0) modes. Figures 11 and 12 illustrate the acoustic pressure field for the monopole and the dipole excitation, respectively, at different frequencies. In Fig. 11(a), for the monopole excitation, the frequency (300 Hz) is below the cutoff of the (0,0) mode, whereby the radiation is expected to show little directionality, as can be confirmed by the plot. Figure 11(b) shows the result at 400 Hz, which is above the cutoff of the (0,0) mode. The radiation shows a clear directionality of the sound field, as expected for operation above cutoff. In addition, the strength of the radiated sound field is much larger than in Fig. 11(a), as also expected since the frequency is above cutoff. When further increasing the frequency to 500 Hz [Fig. 11(c)], the direction of the radiated sound field shifts further toward end-fire, as expected. Note that, in the selected cut plane used for plotting, radiation is also visible on the non-perforated side of the antenna.

In Fig. 12(a), for the dipole excitation, the frequency (1500 Hz) is below the cutoff of the (1,0) mode, whereby the response corresponds to that of the (0,0) mode, showing a plane-wavelike sound field inside the antenna and little directionality outside the antenna, as expected below cutoff. Figure 12(b) shows the result at 2000 Hz, which is above the cutoff of the (1,0) mode. A dipole pattern is visible inside the antenna, which confirms that the (1,0) mode is mainly excited. Outside the antenna, the radiation shows a clear directionality of the sound field, as expected for operation above cutoff. In addition, the strength of the radiated sound field is much larger than in Fig. 12(a). When further increasing the frequency to 2500 Hz [Fig. 12(c)], the direction of the radiated sound field shifts further toward end-fire, as expected.

B. Results from theoretical modeling, finite-element modeling, and measurements

1. Radiation angle and leakage rate as a function of frequency

The resulting radiation angle and leakage rate as functions of frequency are plotted in Figs. 13–16 based on theoretical modeling, finite-element modeling, and measurements of the designed prototype LWA operated by a monopole and a dipole source. The procedure used to determine the radiation angle and leakage rate for each method is described above in the corresponding section.

Comparing the radiation angle results from the theoretical (Theory) and finite-element modeling (COMSOL) in Figs. 13 and 15, a very good agreement is shown, thus successfully validating the finite-element modeling. The results

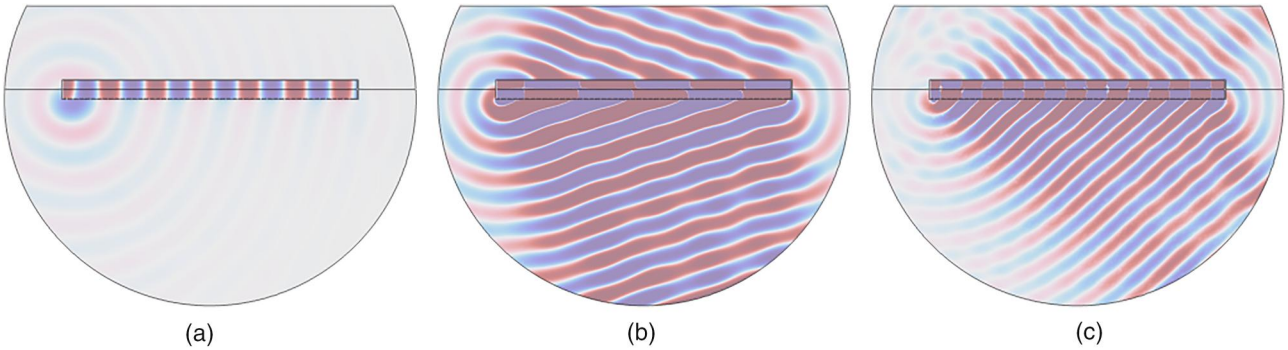

FIG. 12. Plots of the acoustic pressure amplitude (real part) for the antenna operated with a dipole source.

30 October 2026 08:24:33

https://doi.org/10.1121/10.0046796

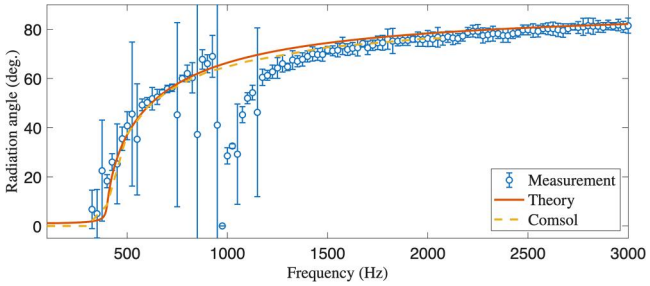

FIG. 13. Radiation angle results from theoretical modeling, finite-element modeling, and measurements, for the antenna with monopole source.

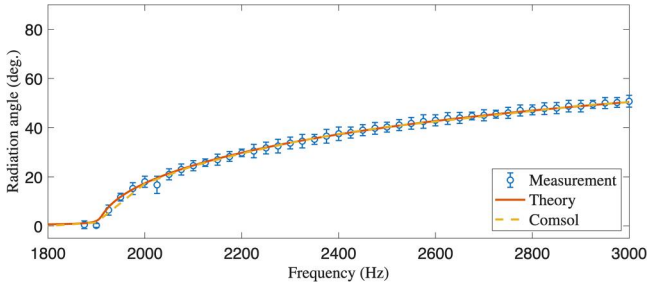

FIG. 15. Radiation angle results from theoretical modeling, finite-element modeling, and measurements, for the antenna with a dipole source.

for the monopole source (Fig. 13) show an abrupt increase in the radiation angle, starting at about 400 Hz. In contrast, the results for the dipole source (Fig. 15) show a more gradual increase in radiation angle as the frequency increases from the onset (at about 1900 Hz) and above, as expected from the theoretical results.

The agreement between the modeled leakage rates obtained from theory and finite-element simulations (Figs. 14 and 16) is good at higher frequencies but deviates in the frequency range where the leakage rate peaks and below, concluded to be due to the finite resolution of the numerical solution.

Concerning the measured results, they are plotted as mean values and estimated 95% confidence intervals in Figs. 13–16. The agreement in radiation angle, with both theory and numerical results, is excellent for the dipole source (Fig. 15) and very good for the monopole source at higher frequencies, above approximately 1500 Hz (Fig. 13). In the lower frequency range from 300 Hz to about 950 Hz, the agreement for the monopole source is good in terms of the measured mean value; however, individual measurements show large discrepancies, as reflected by the large uncertainty. This behavior can be partly attributed to resonances along the length of the antenna, which are allowed to be excited due to the lack of a completely reflection-free termination in the measurement setup. At about 975 Hz, a large deviation from the modeled radiation angle is observed in the measured results. The reason for this is not fully understood, but may be related to a quarter-wavelength resonance in the antenna cross section.

The measured leakage rates generally show very good agreement with the modeled results at higher frequencies (Figs. 14 and 16). In the low-frequency ranges discussed above for the monopole radiation-angle results, the measured leakage rate also deviates. In addition, near the peak of the leakage rate, the measured data also deviate from the theoretical results. This is mainly attributed to measurement uncertainties, which become more influential in leakage-rate estimation because it involves a difference operation [see Eq. (55)].

2. Measured radiation patterns as a function of frequency

To help further understand the radiation performance of the acoustic LWA, the level response as a function of angle and frequency is plotted in Figs. 17 and 18. The dashed lines in the plots show the radiation angle calculated from the theoretical model.

For the monopole source (Fig. 17), the low-frequency response displays a broad and indistinct directivity up to approximately 1000 Hz, where an unexpected lobe appears at broadside (near 0°) and rapidly increases in angle. Above about 1500 Hz, the response displays a less broad, more distinct directivity. These characteristics agree with the discussion above in relation to Fig. 13 and the (0,0) mode. Amplitude variations with peaks separated by about 100 Hz are also observed in the radiation pattern of the (0,0) mode. They are concluded to be attributed to resonances along the length of the antenna, enabled by imperfect termination absorption. At about 1900 Hz, the (1,0) mode begins to emerge, in agreement with the theoretical solution.

For the dipole source (Fig. 18), a distinct directivity is shown from approximately 1900 Hz, in agreement with the theoretical solution for the (1,0) mode. Above about

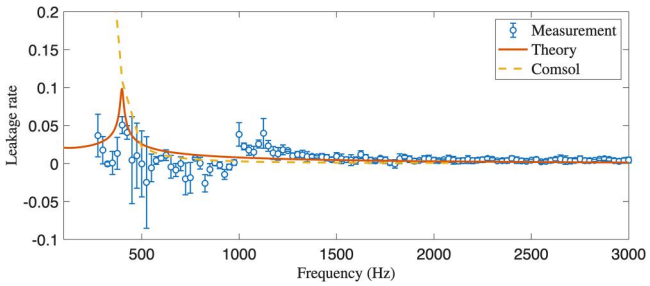

FIG. 14. Resulting leakage factor from theoretical modeling, finite-element modeling, and measurements, for the antenna with a monopole source.

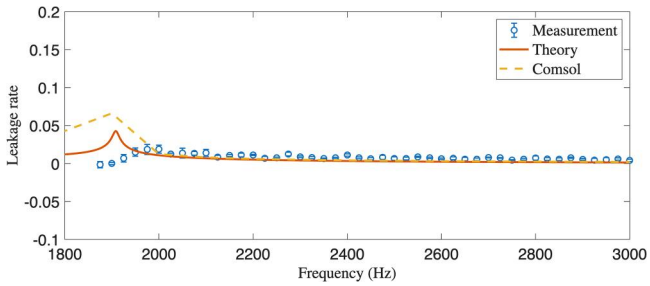

FIG. 16. Resulting leakage factor from theoretical modeling, finite-element modeling, and measurements, for the antenna with a dipole source.

30 October 2026 08:24:33

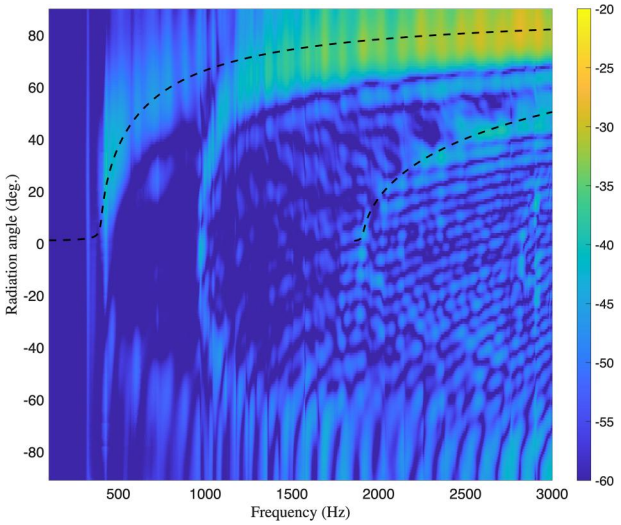

FIG. 17. Response plot of the measured data from the antenna with monopole source. Plotted as radiated pressure in dB (re. arb.) as a function of angle and frequency. Theoretical radiation angle plotted as dashed lines.

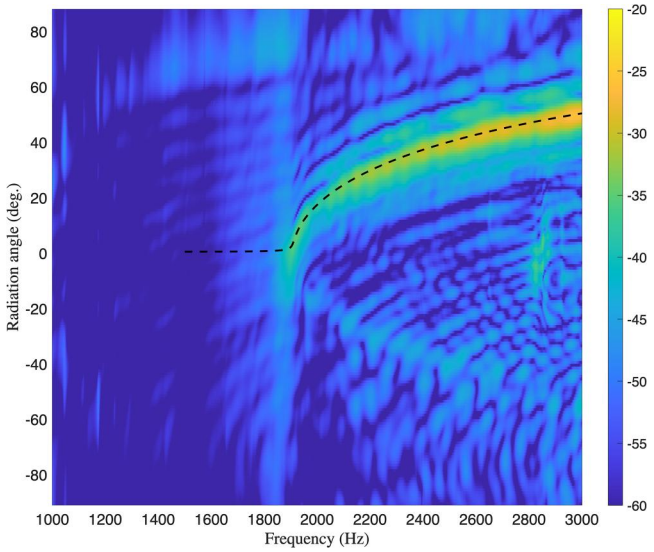

FIG. 18. Response plot of the measured data from the antenna with dipole source.

2000 Hz, sidelobes at angles larger than the mainlobe are clearly visible, and less distinct sidelobes can be seen at angles smaller than the mainlobe. Moreover, it is interesting to note the increase in response at all angles at about 1900 Hz. An explanation for this may be the increased radiation impedance of the source at the onset of the (1,0) mode.

Figure 19 shows directivity plots of the measured data and of the modeled results of the theoretical solution and numerical calculations for the dipole source at frequencies 2, 2.5, and 3 kHz. The theoretical directivity patterns were obtained by assuming a longitudinal aperture distribution proportional to $\exp[-(\alpha + j\beta)z]$ over the finite antenna length L, and computing the far-field radiation pattern from the spatial Fourier transform of this distribution.[24] The results at the three frequencies show excellent agreement in both the direction and the beam width of the mainlobe. The results for the first sidelobes can be seen to agree in angle but show some offsets in relative strength. Moreover, angular agreement for the second sidelobes is visible to some extent. The measured data exhibit additional sidelobes that are not seen in the theoretical solution or in the COMSOL results; the strongest ones can be concluded to be due to

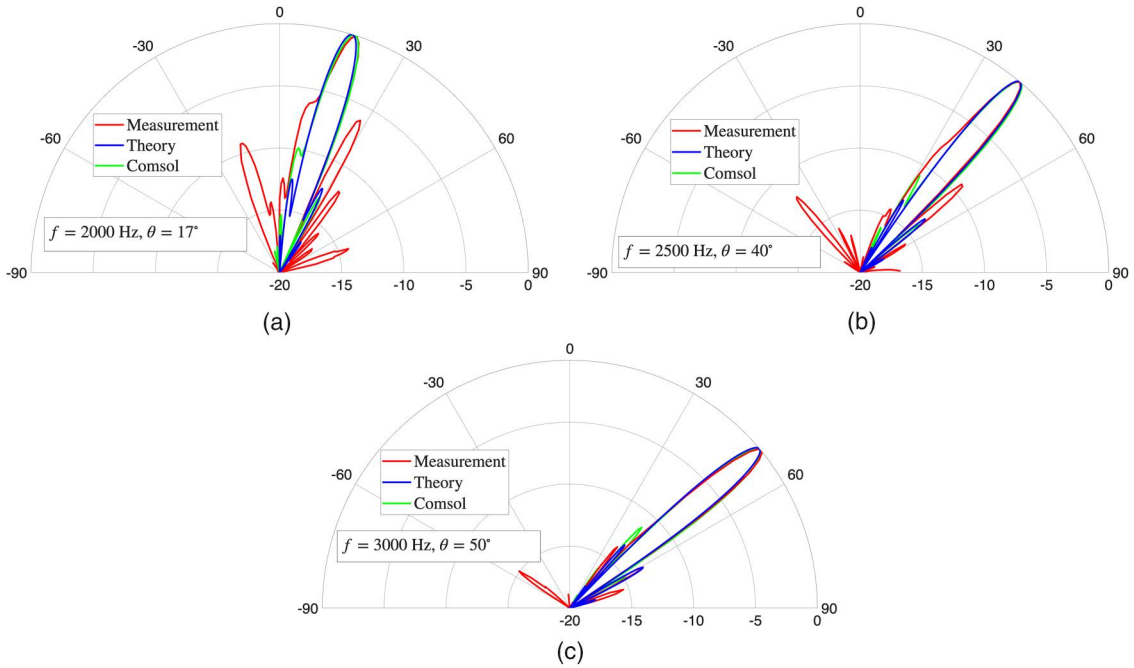

FIG. 19. Directivity plots from measurements, theoretical modeling, and finite-element modeling for the dipole source at frequencies (a) 2 kHz, (b) 2.5 kHz, and (c) 3 kHz. The directivity is normalized to the maximum value for each frequency and plotted within the range from −20 to 0 dB.

30 October 2026 08:24:33

https://doi.org/10.1121/10.0046796

reflection at the termination of the antenna, which is expected to be possible to reduce by using improved absorbers.

The measured results overall support the idea of using the (1,0) mode, with dipole-like excitation, for a frequency-scanning LWA, as it provides good controllability of both the radiation angle and the leakage rate. In addition, the strong agreement between the measured results and the theoretical and numerical predictions of the designed antenna demonstrates a successful validation of the modeling.

V. CONCLUSION

The paper presents consistent theoretical modeling, numerical modeling, and measurements of a designed and built acoustic LWA. The results show proof of concept of the ALWA with frequency scanning capability, i.e., that the radiation angle can be controlled by the frequency of the source (the feeding of the antenna).

The presented theory provides the necessary formulations for predicting the two main design parameters, the radiation angle and leakage rate, for uniform or quasi-uniform ALWAs. The central parts of the theory include the TEN, the TRE, and the solution of the TRE via the resonance condition on reflection factors, which results in the real and imaginary parts of the longitudinal wavenumber. For the acoustical setting of hard boundaries, the existence of the (0,0) mode, i.e., a static mode, was identified. Theoretical steps also include a description of the modal solution and of the shapes of the two lowest modes, i.e., mode (0,0) and mode (1,0), as well as the impedance modeling of the perforated wall of the antenna. The developed theoretical model was used for parameter studies of the perforation hole radius and cross-sectional width of the antenna. The results indicated that using the (1,0) mode could be preferable to using the (0,0) mode for frequency scanning due to greater controllability of the radiation angle and leakage rate.

Wave-based modeling is performed using the FEM, with validity supported by good agreement with the theoretical model in terms of radiation angle and leakage rate for the two modes studied. The validated numerical tool is particularly useful for modeling more complex antenna designs, for example those with non-uniform variations along the antenna length.

Based on the theoretical and numerical results, a prototype antenna was designed and built for use in validating measurements. A source with either monopole or dipole characteristics was used to mainly excite the (0,0) mode or the (1,0) mode, respectively. The measured data showed very good agreement with the modeled results for the radiation angle for the (1,0) mode, while the (0,0) mode showed significant deviations within a range of lower frequencies. The general agreement in leakage rate was good, except for larger deviations below and near the peak frequency.

Taken together, the measurement results confirm the validity of the theoretical and numerical modeling, as well as the good frequency-scanning capability of the designed prototype ALWA for the (1,0) mode. For future work, further studies of ALWA behavior and investigations of more complex ALWA designs are of interest, including modulated or tapered geometries for controlling, e.g., sidelobe levels and beam shape, as well as the incorporation of resonant elements to enable backward-to-forward beam scanning.

ACKNOWLEDGMENTS

The work of Astrid Algaba-Brazález is supported by the Grant RYC2022-037385-I funded by MICIU/AEI/10.13039/501100011033 and by ESF+. The work of José Luis Gómez-Tornero, Pablo-Antonio Martínez-Vicente and Astrid Algaba-Brazález is also supported by the Spanish National Project under Grant PID2022-136590OB-C42 funded by MICIU/AEI/10.13039/501100011033 and by FEDER, UE. The research work disclosed in this publication is partially funded by the ENDEAVOR II Scholarships Scheme (Malta). Project may be co-funded by the ESF+ 2021–2027.

AUTHOR DECLARATIONS

Conflict of Interest

The authors have no conflicts to disclose.

DATA AVAILABILITY

The data that support the findings of this study are available within the article.

[1]W. W. Hansen, "Radiating electromagnetic wave guide," U.S. patent 2,402,622 (1946).
[2]D. Jackson and A. Oliner, "Ch. 7: Leaky-wave antennas," in *Modern Antenna Handbook* (Wiley, Hoboken, NJ, 2008).
[3]D. R. Jackson, C. Caloz, and T. Itoh, "Leaky-wave antennas," Proc. IEEE **100**(7), 2194–2206 (2012).
[4]D. Jackson, P. Burghignoli, G. Lovat, F. Capolino, J. Chen, and D. Wilton, "The fundamental physics of directive beaming at microwave and optical frequencies and the role of leaky waves," Proc. IEEE **99**(10), 1780–1805 (2011).
[5]C. J. Naify, M. D. Guild, C. A. Rohde, D. C. Calvo, and G. J. Orris, "Demonstration of a directional sonic prism in two dimensions using an air-acoustic leaky wave antenna," Appl. Phys. Lett. **107**(13), 133505 (2015).
[6]C. J. Naify, J. S. Rogers, M. D. Guild, C. A. Rohde, and G. J. Orris, "Evaluation of the resolution of a metamaterial acoustic leaky wave antenna," J. Acoust. Soc. Am. **139**(6), 3251–3258 (2016).
[7]C. J. Naify, M. Haberman, M. Guild, and C. Sieck, "Acoustic leaky wave antennas: Direction-finding via dispersion," Acoust. Today **14**(3), 31–38 (2018).
[8]Q. Wang, J. Lan, Z. Deng, Y. Lai, and X. Liu, "Acoustic leaky-wave antennas with heterogeneous unit cells for enhanced directivity and localization," J. Acoust. Soc. Am. **153**(1), 487–495 (2023).
[9]H. Esfahlani, S. Karkar, H. Lissek, and J. R. Mosig, "Acoustic dispersive prism," Sci. Rep. **6**(1), 18911 (2016).
[10]H. Esfahlani, S. Karkar, H. Lissek, and J. R. Mosig, "Exploiting the leaky-wave properties of transmission-line metamaterials for single-microphone direction finding," J. Acoust. Soc. Am. **139**(6), 3259–3266 (2016).
[11]I. Felis-Enguix, J. Otero-Vega, M. Campo-Valera, I. Villó-Pérez, and J. L. Gómez-Tornero, "Practical aspects of acoustic leaky-wave antennas applied to underwater direction finding," Eng. Proc. **2**(1), 93 (2020).

30 October 2026 08:24:33

[12]M. Poveda-García, D. Cañete-Rebenaque, and J. L. Gómez-Tornero, "Frequency-scanned monopulse pattern synthesis using leaky-wave antennas for enhanced power-based direction-of-arrival estimation," IEEE Trans. Antennas Propag. **67**(11), 7071–7086 (2019).
[13]J. L. Gómez-Tornero, "Smart leaky-wave antennas for iridescent IoT wireless networks," in *Antenna and Array Technologies for Future Wireless Ecosystems* (Wiley, 2022), pp. 119–181.
[14]J. A. López-Pastor, M. Poveda-García, A. Gil-Martínez, D. Cañete-Rebenaque, and J. L. Gómez-Tornero, "2-D localization system for mobile IoT devices using a single Wi-Fi access point with a passive frequency-scanned antenna," IEEE IoT. J. **10**(17), 14995–15011 (2023).
[15]T. Fukushima, T. Matsukawa, Y. Ikemura, H. Terasoma, S. Kato, T. Fujihashi, T. Murakami, Y. Asai, and S. Saruwatari, "Wi-Fi meets sound: A deep fusion leap beyond single-modality for device localization," IEEE Access **13**, 170291–170306 (2025).
[16]C. J. Naify, C. N. Layman, T. P. Martin, M. Nicholas, D. C. Calvo, and G. J. Orris, "Experimental realization of a variable index transmission line metamaterial as an acoustic leaky-wave antenna," Appl. Phys. Lett. **102**(20), 203508 (2013).
[17]J. Lan, X. Peng, X. Zhang, X. Liu, and Y. Li, "Improving directional radiation quality based on a gradient amplitude acoustic leaky wave antenna," New J. Phys. **21**(10), 103023 (2019).
[18]C. W. Broadman, C. J. Naify, M. J. Lee, and M. R. Haberman, "Design of a one-dimensional underwater acoustic leaky wave antenna using an elastic metamaterial waveguide," J. Appl. Phys. **129**(19), 194902 (2021).
[19]J. Zhang, V. Romero-García, G. Theocharis, O. Richoux, V. Achilleos, and D. J. Frantzeskakis, "High-amplitude sound propagation in acoustic transmission-line metamaterial," Appl. Phys. Lett. **118**(10), 104102 (2021).
[20]A. Fernández-Garrido, M. Campo-Valera, E. Abdo-Sánchez, R. Picó, A.-J. Garcia-Sanchez, and R. Asorey-Cacheda, "Parametric study and experimental validation of acoustic leaky wave antenna in spatial localization," IEEE Access **13**, 10371–10385 (2025).
[21]COMSOL AB, "COMSOL Multiphysics® acoustics module [version 6.2]," https://www.comsol.com/acoustics-module (last viewed, 20 May 2025).
[22]T. Zhao, D. R. Jackson, J. T. Williams, and A. A. Oliner, "General formulas for 2-d leaky-wave antennas," IEEE Trans. Antennas Propag. **53**(11), 3525–3533 (2005).
[23]J. Hines and J. Upson, "A wide aperture tapered-depth scanning antenna," Ohio State Univ. Res. Found **667**, 10 (1957).
[24]A. A. Oliner, D. R. Jackson, and J. Volakis, "Leaky-wave antennas," Antenna Eng. Handbook **4**, 12 (2007).
[25]R. Sorrentino and M. Mongiardo, "Transverse resonance techniques," in Encycloped. RF Microwave Eng. (Wiley, 2005).
[26]J. L. Gómez-Tornero, J. Pascual-García, and A. Álvarez-Melcón, "A novel full-wave CAD for the design of tapered leaky-wave antennas in hybrid waveguide printed-circuit technology," Int. J. RF Microwave Comput. Aided Eng. **16**(4), 297–308 (2006).
[27]M. Garcia-Vigueras, J. L. Gomez-Tornero, G. Goussetis, A. R. Weily, and Y. J. Guo, "Efficient synthesis of 1-D Fabry–Perot antennas with low sidelobe levels," IEEE Antennas Wirel. Propag. Lett. **11**, 869–872 (2012).
[28]A. J. Martinez-Ros, J. L. Gómez-Tornero, and F. Quesada-Pereira, "Efficient analysis and design of novel SIW leaky-wave antenna," IEEE Antennas Wirel. Propag. Lett. **12**, 496–499 (2013).
[29]L. E. Kinsler, A. R. Frey, A. B. Coppens, and J. V. Sanders, *Fundamentals of Acoustics*, 4th ed. (John Wiley & Sons, New York, 1999).
[30]C. Caloz and T. Itoh, *Radiated Wave Applications* (John Wiley & Sons, New York, 2005), pp. 261–315.
[31]M. Poveda-García, A. Algaba-Brazalez, and J. L. Gómez-Tornero, "Impact of reactive phenomena on performance of uniform leaky-wave antennas, in press," IEEE Trans. Antennas Propag. 1 (2026).
[32]M. Poveda-García, A. Algaba-Brazalez, D. Comite, and J. L. Gómez-Tornero, "Impact of the reactive attenuation constant in the efficiency of uniform/quasi-uniform leaky-wave antennas radiating at broadside," in *Proceedings of the International Conference on Electromagnetics in Advanced Applications (ICEAA 2025)*, Palermo, Italy (2025).
[33]I. Mann, J. Adin, J. Tichy, and A. J. Romano, "Instantaneous and time-averaged energy transfer in acoustic fields," J. Acoust. Soc. Am. **82**(1), 17–30 (1987).
[34]T. E. Vigran, *Building Acoustics* (CRC Press, Boca Raton, FL, 2008), p. 362.
[35]M. Kleiner, *Electroacoustics* (Taylor & Francis Group, London, 2013).
[36]R. T. Randeberg, "Perforated panel absorbers with viscous energy dissipation enhanced by orifice design," Ph.D. thesis, Department of Telecommunications, Norwegian University of Science and Technology, Trondheim, Norway (2000).
[37]R. L. Pritchard, "Mutual acoustic impedance between radiators in an infinite rigid plane," J. Acoust. Soc. Am. **32**(6), 730–737 (1960).
[38]H. Lin, T. Bengisu, and Z. P. Mourelatos, *Lecture Notes on Acoustics and Noise Control* (Springer, New York, 2023).
[39]F. Bongard, H. Lissek, and J. R. Mosig, "Acoustic transmission line metamaterial with negative/zero/positive refractive index," Phys. Rev. B **82**, 094306 (2010).
[40]The MathWorks, Inc., "*fminsearch*," https://www.mathworks.com/help/optim/ug/fminsearch.html (Last viewed 20 May 2025).
[41]COMSOL, "Perfectly matched boundary," https://doc.comsol.com/6.0/doc/com.comsol.help.aco/aco_ug_pressure.05.035.html (Last viewed 20 May 2025).
[42]COMSOL, "External field calculation," https://doc.comsol.com/5.5/doc/com.comsol.help.aco/aco_ug_pressure.05.024.html (Last viewed 20 May 2025).
[43]COMSOL, "Sound hard boundary," https://doc.comsol.com/5.5/doc/com.comsol.help.aco/aco_ug_pressure.05.067.html (Last viewed 20 May 2025).
[44]D. I. Havelock, S. Kuwano, and M. Vorländer, *Handbook of Signal Processing in Acoustics* Vol. 1 (Springer, New York, 2008).
[45]S.-T. Yang and H. Ling, "Two-section half-width microstrip leaky wave antenna," IEEE Trans. Antennas Propag. **62**(10), 4988–4996 (2014).

30 October 2026 08:24:33